Article

Self-Adaptive Flask-like Nanomotors Based on Fe_3O_4 Nanoparticles to a Physiological pH

Tianyu Gao, Jinwei Lin, Leilei Xu * and Jianguo Guan *

State Key Laboratory of Advanced Technology for Materials Synthesis and Processing, School of Materials Science and Engineering, Wuhan University of Technology, Wuhan 430070, China; gty@whut.edu.cn (T.G.); linjinwei@whut.edu.cn (J.L.)

* Correspondence: xull@whut.edu.cn (L.X.); guanjg@whut.edu.cn (J.G.)

Abstract: In living bodies, pH values, which are precisely regulated and closely associated with diseased cells, can act as an efficient biologically intrinsic indicator for future intelligent biomedicine microsystems. In this work, we have developed flask-like carbonaceous nanomotors (FCNMs), via loading Fe_3O_4 nanoparticles (NPs) into a cavity, which exhibit a self-adaptive feature to a specific physiological pH by virtue of the pH-dependent dual enzyme-like activities of Fe_3O_4 NPs. Specifically, the peroxidase-like activity of Fe_3O_4 NPs in an acidic pH range, and the catalase-like activity in a near neutral and alkaline pH range, determine the products in the motion system (●OH, ions and O_2), whose diffusions from the inner to the outside of the flask result in fluid movement providing the driving force for the movement of the FCNMs. Correspondingly, changes of the product concentrations and species in the physiological pH range (4.4–7.4) result, firstly, in velocity decrease and, then, with increase in pH, increase of the FCNMs occurs. Thanks to the non-linear velocity responsiveness, the FCNMs show intriguing pH taxis towards 6.8 (generally corresponding to the physiological pH in tumor microenvironments), where a maximum velocity appears. Furthermore, the superparamagnetic feature of the Fe_3O_4 NPs simultaneously endows the FCNMs with the abilities to be magnetic-oriented and easily separated. This work could significantly increase the possibility of nanomotors for targeted therapy of tumors and next-generation biotechnological applications.

Keywords: nanomotors; pH responsiveness; Fe_3O_4 nanoparticles; dual enzyme-like activities; physiological pH chemotaxis

1. Introduction

Micro/nanomotors (MNMs), inspired by natural microorganisms, are artificial power devices between nano- and micro-scale that can convert energy in the environment into efficient motion [1]. Their excellent movement characteristics, especially when moving in micro-scale regions or enclosed areas, and chemically rich features show great promise for the revolutionization of biomedical applications [2–11].

Smart drug delivery with active targeting abilities is essential for futuristic biomedical fields. Compared with external field-propelled MNMs, chemically driven MNMs can harvest energy from their surroundings to induce movement, which provides a possibility for responding to local environments. In recent years, a growing effort has been devoted to engineer diverse chemically driven MNMs to respond to various stimuli, including metabolite concentration [12,13], microenvironment temperature [14,15], etc. In living bodies, pH value is an efficient biologically intrinsic indicator because it is highly diverse and precisely regulated in different organs and tissues. For example, the extracellular pH for healthy human tissues varies around 7.4, whereas the pH in tumor microenvironments is marginally acidic, ranging from 6.5 to 7.0 (average ~6.8), which further drops to 4.4–6.0 within tumor cells [16]. Minor changes of pH values in specific areas may affect physiological metabolism and even lead to diseases. Therefore, the various pH values

can act as chemical signals to induce the responsive motion of MNMs. For example, the pH-responsive MNMs fabricated by catalytic materials, such as bio-enzymes [17], nano-enzymes [18–21] or active metals [22–26], the catalytic activities of which are influenced by environmental pH, usually show change of velocities and directions upon regulating the "fast/slow" aspect of pH-dependent driving reactions. Introducing pH-responsive polymers into MNMs, as gatekeepers to regulate the accessibility of "fuel", also easily achieve "on/off" of MNMs [21,27]. Additionally, pH-induced hydrophilicity/hydrophobicity transition and surface tension variation are also used to control the motion of MNMs displaying pH-responsiveness [28,29]. Although some well-designed MNMs can display a responsive motion behavior using pH as an indicator, the responsiveness levels are only indicated by monotonous velocity changes or transient on/off. However, besides simply identifying their microenvironments, the self-adaptive movement of MNMs to a specific pH, like some microorganisms with chemotaxis that are able to autonomously move to specific areas, is indispensable for futuristically smart motor systems. It means that they are able to seek focal sites in terms of a specific pH actively, and thus realize targeted drug delivery toward tumors.

Herein, we designed and constructed flask-like carbonaceous nanomotors (FCNMs) that exhibit self-adaptive pH-responsive motion behavior in the physiological pH range (4.4–7.4) on the basis of pH-dependent dual enzyme-like activities of Fe_3O_4 NPs. The non-monotonic change of velocities for as-prepared FCNMs are influenced by the diffusion behaviors of pH-dependent products. At a lower pH range (4.4–5.6), Fe_3O_4 NPs show peroxidase-like activity and the FCNMs are propelled by the diffusion of the product ●OH and ions from the buffer solution used to balance the pH value of the system. With increase of the pH values, the peroxidase-like activity decreases until it disappears, while the catalase-like activity of Fe_3O_4 NPs appears and increases. This leads to the transformation of the driving mechanisms from ionic and non-ionic diffusiophoresis to non-ionic diffusiophoresis. Correspondingly, the as-prepared FCNMs show a maximum motion velocity of 12.4 body lengths s^{-1} at pH 6.8 within 20 mM buffer solution and a fantastically spontaneous pH-chemotaxis from 7.4 to 6.8, which has a tempting application prospect for targeting tumor microenvironments. Additionally, thanks to the superparamagnetism of Fe_3O_4 NPs, long-range motion control of the FCNMs is easily achieved by a magnetic field. These findings provide some insights into the pH-responsive motion mechanisms of Fe_3O_4-based MNMs, and offer some possibilities for application in biomedical fields, especially in the targeted therapy of tumors.

2. Materials and Methods

2.1. Materials and Reagents

Iron chloride ($FeCl_3 \cdot 6H_2O$, ≥98%), oleic acid (OA, 85%), dimethylsulfoxide (DMSO, ≥99.5%), triethylamine (≥99%), acetone, n-hexane, chloroform and ethanol were purchased from TCI (Shanghai, China) Development Co., Ltd., China. Oleyl alcohol (80~85%) was purchased from Weng Jiang Reagent Co., Ltd. (Guangdong, China). Sodium oleate ($C_{17}H_{33}CO_2Na$, >97%), dimercaptosuccinic acid (DMSA, 98%) and diphenyl ether (>99%) were purchased from Aladdin Biochemistry Co., Ltd. (Shanghai, China). D-ribose (≥98%) and poly(ethylene glycol)-block-poly(propylene glycol)-block-poly(ethylene glycol) (EO_{20}-PO_{70}-EO_{20}, P123) were purchased from Sigma-Aldrich (Shanghai, China). Deionized water was produced in a Milli-Q system (Millipore, MA, USA) for the preparation of all aqueous solutions.

2.2. Synthesis of Fe₃O₄@OA NPs

The Fe_3O_4@OA NPs were synthesized according to previously reported procedure, with a slight modification [30]. Briefly, 3.6 g of Fe(oleate)$_3$ precursor, 1.14 g of oleic acid, and 3.22 g of oleyl alcohol were dissolved in 20 g of diphenyl ether at room temperature. The mixture was first heated to 90 °C at a constant heating rate of 8 °C/min in a nitrogen atmosphere, kept for 2 h to remove dissolved oxygen, and then heated to 220 °C to maintain

this temperature for 10 min. After the reaction, the mixed solution was quickly cooled to room temperature, and the nanoparticles were washed three times with a mixed solvent of acetone and n-hexane by centrifugal separation, and finally dispersed in chloroform.

2.3. Modification of Fe_3O_4@OA NPs by DMSA

Fe_3O_4@DMSA NPs was prepared according to the previously reported method [31]. Briefly, 100 mg Fe_3O_4@OA NPs were first dispersed in 10 mL chloroform and 50 μL triethylamine were added. Next, 50 mg DMSA was dissolved in 10 mL DMSO and added to the above solution. The resulting mixed solution was magnetically stirred vigorously for 12 h at 60 °C. Then, the nanoparticles were washed three times with ethanol by centrifugal separation. In order to modify more DMSA on the surface of the Fe_3O_4 NPs, and improve the water solubility, the nanoparticles were once again dispersed in ethanol for surface double-exchange. After repeating the previous operation, the obtained Fe_3O_4@DMSA NPs were washed with deionized water and dispersed in it.

2.4. Synthesis of Flask-like Carbonaceous Carriers (FCCs)

FCCs were prepared according to the previously reported method [32,33]. Briefly, 0.0365 g of sodium oleate and 0.0435 g of P123 were dissolved in 20 mL deionized water and stirred slowly for a period of time at 40 °C until it became clarified. Next, 40 mL aqueous solution, containing 3 g D-ribose, was added to the above solution. The mixed solution was transferred to a 100 mL autoclave and hydrothermally treated at 160 °C for 12 h. Then, the resulting FCCs were washed with deionized water three times.

2.5. Preparation of FCNMs

A certain number of dry FCCs were added to the water/ethanol mixed solution containing Fe_3O_4@DMSA NPs. Next, the mixture was treated in an ultrasonic instrument for 20 min to allow the FCCs to be fully dispersed and the Fe_3O_4@DMSA NPs to enter the hollow structure. The excess Fe_3O_4@DMSA NPs were removed by repeated washing and centrifugation until the supernatant was transparent. Then, the obtained products were placed in a vacuum drying oven at 60 °C for 12 h. The procedure was repeated three times and, finally, the resulting FCNMs were scattered in the deionized water.

2.6. Observation of the Motion of the FCNMs

The motion of the as-prepared FCNMs was observed by using a Leica DM 3000B optical microscope with a high-resolution CCD digital camera at a frame rate of 18 fps. For exploring the influence of pH values on motion behaviors, the H_2O_2 concentration of the whole system was diluted to 2.5 wt%, and their pH values were adjusted to 4.4, 5.0, 5.6, 6.2, 6.8 and 7.4 using 20 mM disodium hydrogen phosphate-citrate buffer solution. For studying the influence of H_2O_2 concentrations on motion behaviors, concentrations of 0.5 wt%, 1 wt%, 2.5 wt%, 5 wt% and 10 wt% were adopted, respectively. For the spontaneous chemotactic experiments, agar (0.5 cm × 0.5 cm) was put in 2.5 wt% H_2O_2 solution (pH 6.8) for 12 h at room temperature in advance, then taken out and put on a hydrophobic glass substrate. Subsequently, 2.5 wt% H_2O_2 solution (pH 7.4), containing the FCNMs, was dropped on the other side. For the magnetic manipulation experiments for the FCNMs, 2.5 wt% H_2O_2 solution (pH 6.8), containing the FCNMs, was dropped on a hydrophobic glass substrate, and the direction of its motion was manipulated by moving an external magnet.

2.7. Characterization

The scanning electron microscope (SEM) images were taken with a Hitachi S-4800 microscope (Tokyo, Japan). The transmission electron microscopy (TEM) and energy-dispersive X-ray (EDX) images were taken with a FEI F200 microscopy (Hillsboro, OR, USA). The powder X-ray diffraction (XRD) patterns were obtained with a Empyrean diffractometer (Almelo, Holland). Magnetic properties were analyzed with a Lake Shore

7400 vibrating sample magnetometer (VSM, Westerville, OH, USA). The thermal properties were evaluated with a STA 449F3 thermogravimeter (TG, Selb, Germany). The dynamic light scattering (DLS) measurements were proceeded with a NanoBrook 90Plus Zeta (New York, NY, USA). The motion videos and images were recorded with a Leica DM 3000B optical microscope (Wetzlar, Germany).

2.8. Numerical Simulation

Our numerical model was implemented in COMSOL Multiphysics (version 5.4a) in a 2D axisymmetric configuration to reduce the computational cost. The primary model parameters are shown in Table S1 and Figure S1 in the Supplementary Materials. The chemical reaction engineering and dilute chemical species transport module were employed. Fe_3O_4 NPs were presumed to distribute uniformly in the flask bottom with a constant concentration of 7.14×10^{-5} mol·m^{-2}. When the FCNMs moved in an acid condition (pH 4.4), chemical reactions: $\equiv Fe^{2+} + H_2O_2 \rightarrow \equiv Fe^{3+} + OH^- + \bullet OH$ and $OH^- + C_6H_8O_7 \leftrightarrows C_6H_7O_7^- + H_2O$ occurred in the confined cavity, which were calculated by a chemical reaction engineering model with a rate constant of 65 M^{-1}·s^{-1} and 1.1×10^{10} M^{-1}·s^{-1}, respectively, and the governing equation was as follows:

$$\frac{dc_i}{dt} = R_i + R_{ads,i}\frac{A_r}{V_r} \tag{1}$$

Here, for a species i, c_i is the concentration, R_i is the rate of the species, $R_{ads,i}$ is the surface reaction area, and V_r is the reactor volume. Transport of diluted species is used to compute the concentration field with the governing equation:

$$\nabla J_i = u\nabla c_i - D_i\nabla^2 c_i \tag{2}$$

where J_i and c_i are the ionic flux and ionic concentration for species *i*, respectively, *u* is the flow velocity, *D* is the ionic diffusion coefficient. We noted that diluted species distributions were affected by flow field and chemical potential field. Chemical reaction: $OH^- + C_6H_8O_7 \leftrightarrows C_6H_7O_7^- + H_2O$ took place in fluid bulk. Rather, the reaction: $\equiv Fe^{2+} + H_2O_2 \rightarrow \equiv Fe^{3+} + OH^- + \bullet OH$ took place on the catalytic surface, and the boundary fluxes at the catalytic surfaces thus became:

$$n\cdot(-D_i\nabla c_i) = R_{ads,i} \tag{3}$$

The FCNM was driven by both chemical potential fields generated by concentrations of ionic species and non-ionic species, respectively. As the FCNM was fixed in the model, we set the FCNM surface as the slip boundary condition, and combined chemiosmotic flow, with a slip velocity, as:

$$\begin{aligned} u &= u_{ionic} + u_{non-ionic} \\ &= (I - nn)(b_{p\_ionic}\cdot\textstyle\sum(\nabla c_{ions}) + b_{p\_non-ionic}\cdot\textstyle\sum(\nabla c_{non-ions})) \end{aligned} \tag{4}$$

where b_{p_ionic} and $b_{p\_non-ionic}$ are the surface mobility of the FCNM, caused by concentrations of ionic species and non-ionic species. On account of solvation of ions, b_{p_ionic} and $b_{p\_non-ionic}$ have opposite signs, which means opposite direction of flow. And the quantity $(I - nn)$ defines the concentration gradients, where *I* denotes the second-order unit tensor. Fluid field around the FCNM was solved by Stokes equation:

$$\nabla p = \eta\nabla^2 u, \ \nabla\cdot u = 0 \tag{5}$$

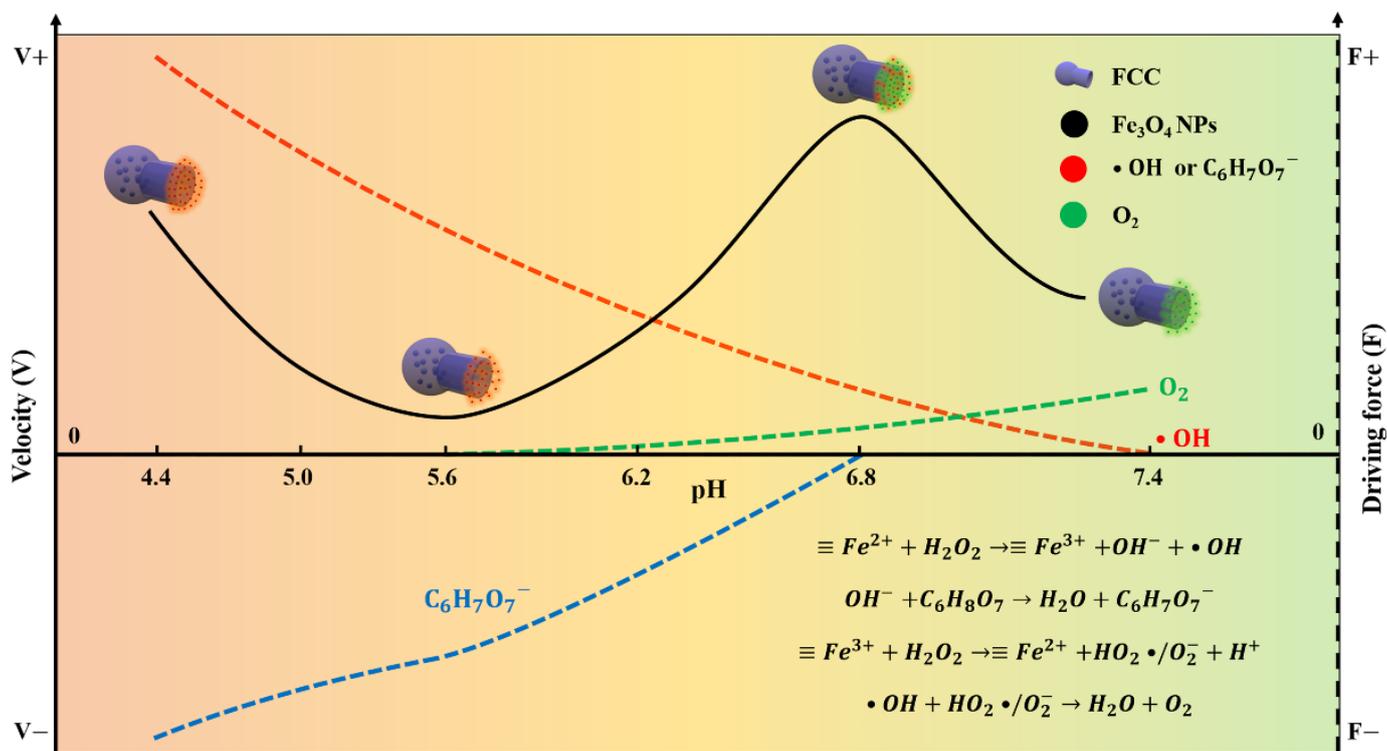where *p* is the pressure, η is dynamic viscosity of water.
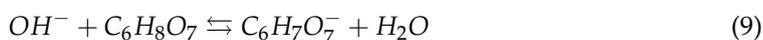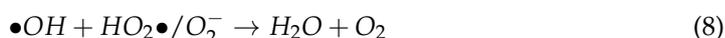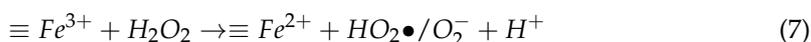
When the FCNMs moved in a near alkaline condition (pH 7.4), the chemical potential field caused by ∇c_{O_2} was considered the main source of driving force. The boundary conditions at the outer edge of the simulation domain were chosen to represent the bulk:

constant concentrations of species, and a no stress boundary condition for fluid. At the FCNMs' surfaces, we prescribed a uniform charge density. We solved for transient state for the FCNMs, which shows the system reached a stable state after 1 ms, hence, results in the discussion all are at 1 ms.

3. Results and Discussion

3.1. Implementation Strategy of the pH-Responsive FCNMs

The self-adaptive physiological pH-responsive FCNMs were realized by virtue of the dual-enzyme catalytic reactions of Fe_3O_4 NPs for H_2O_2 decomposition inside the confined cavity of flask-like structures (Figure 1). When Fe_3O_4 NPs encountered the catalyzed substrate of H_2O_2, the following reactions occurred:

$$\equiv Fe^{2+} + H_2O_2 \rightarrow \equiv Fe^{3+} + OH^- + \bullet OH \tag{6}$$

$$\equiv Fe^{3+} + H_2O_2 \rightarrow \equiv Fe^{2+} + HO_2\bullet/O_2^- + H^+ \tag{7}$$

$$\bullet OH + HO_2\bullet/O_2^- \rightarrow H_2O + O_2 \tag{8}$$

$$OH^- + C_6H_8O_7 \leftrightarrows C_6H_7O_7^- + H_2O \tag{9}$$

Figure 1. Schematic of the self-adaptive pH-responsive motion behaviors of the as-prepared FCNMs based on the pH-dependent catalytic activities of Fe_3O_4 NPs. The velocity and driving force toward the flask mouth direction were set to be positive (V+ and F+). At a lower pH value, the FCNMs were driven by the co-effect of $C_6H_7O_7-$ and $\bullet OH$ diffusiophoresis in the opposite directions. With the reduction of ionic diffusiophoresis and the addition of O_2 diffusiophoresis, the motion velocity increased in the weak acid environment. In the near alkaline range, O_2 diffusiophoresis provided the driving force for the FCNMs showing a reduction of the velocity.

At a lower pH (e.g., pH < 5.6 in Figure 1), Equation (6) dominated with a rate constant of 65 $M^{-1} \cdot s^{-1}$ to produce •OH, and Equations (7) and (8) were inhibited because of the acidity of the solution, indicating its peroxidase-like activity. To eliminate the effect of ion by-products on the pH value, all motions of the as-prepared FCNMs were observed in a 20 mM buffer solution. At this time, the FCNMs were driven by the co-effect of $C_6H_7O_7^-$ and •OH diffusiophoresis in the opposite directions. With increasing pH to near neutral or alkaline, Equation (7) was the rate-determining step (k = 2.5 × 10^{-3} $M^{-1} \cdot s^{-1}$) was promoted, and O_2 was produced instead of •OH (Equation (8)). This could lead to the driving force having to convert into O_2 diffusiopheresis. Therefore, with increasing pH in the acidic environment (pH < 5.6), the decrease of peroxidase-like activity could reduce the concentrations of $C_6H_7O_7^-$ and •OH, and, thus, decrease the motion velocity of the FCNM. On further increasing pH from 5.6 to 6.8, the diffusiophoresis of $C_6H_7O_7^-$ was weakened until it disappeared, because the occurrence of Equations (7) and (8) decreased the concentration of $C_6H_7O_7^-$ via producing H^+ to neutralize OH^-, and simultaneously generated O_2 for driving the FCNMs. This resulted in increase of the moving velocity. When pH > 6.8, the catalase-like activity of Fe_3O_4 dominated instead of peroxidase-like activity and O_2 diffusiophoresis acted as the main driving force. Due to the relatively low-rate constant of Equation (7), the concentration of O_2 was lower in the system and the velocity decrease might have also been due to the diffusion restriction of the flask-like structures. As a result, the as-prepared FCNMs displayed self-adaptive motion behaviors following the pH changes in the system.

3.2. Preparation and Characterization of the FCNMs

The FCNMs were prepared by loading Fe_3O_4@DMSA NPs in flask-like carbonaceous carriers (FCCs), as schematically illustrated in Figure 2a. The FCCs were synthesized by a soft-template-assisted hydrothermal method with a relatively uniform size of 600 nm, a cavity of ~280 nm and a flask mouth of ~140 nm (Figure S2). Their surfaces were rich in hydroxyl and carboxyl groups giving rise to a lower surface potential (−57 mV). Then, using the thermal decomposition method, different Fe_3O_4@OA NPs were synthesized by regulating experimental parameters, including aging temperature (Figure S3), aging time (Figure S4) and raw material molar ratios (Figure S5). The results indicated that the as-synthesized nanoparticles were magnetite (Fe_3O_4; JCPDS no. 75-0033) with a cubic inverse spinel structure, and simultaneously, it could also be found that the particle size and saturation magnetization increased with increasing aging temperature, time or decreasing the amount of oleyl alcohol. Subsequently, the nanoparticles with the highest catalytic activity (Figure S6 and Table S2) were modified by DMSA to achieve transformation from hydrophobicity to hydrophilicity (Figure S7). Next, the morphology and structure of the as-prepared FCNMs were characterized by SEM (Figure 2b) and TEM (insert), showing smooth outer surfaces and large inner cavities with particles. The EDX images shown in Figure 2c clearly confirmed the loading of the Fe_3O_4 NPs in the cavity of the FCCs. The XRD patterns (Figure 2d) further verified that the FCNMs were composed of amorphous FCCs and Fe_3O_4 NPs. The loading amount of Fe_3O_4 NPs was evaluated to be 10.22% by TG (Figure 2e). The saturation magnetization of the FCNMs was 7.4 $emu \cdot g^{-1}$, which was much lower than that of Fe_3O_4 NPs (40.9 $emu \cdot g^{-1}$, Figure 2f), with no hysteresis, demonstrating their superparamagnetic features favoring magnetic field manipulation. Overall, Fe_3O_4-based flask-like carbonaceous nanomotors were successfully constructed.
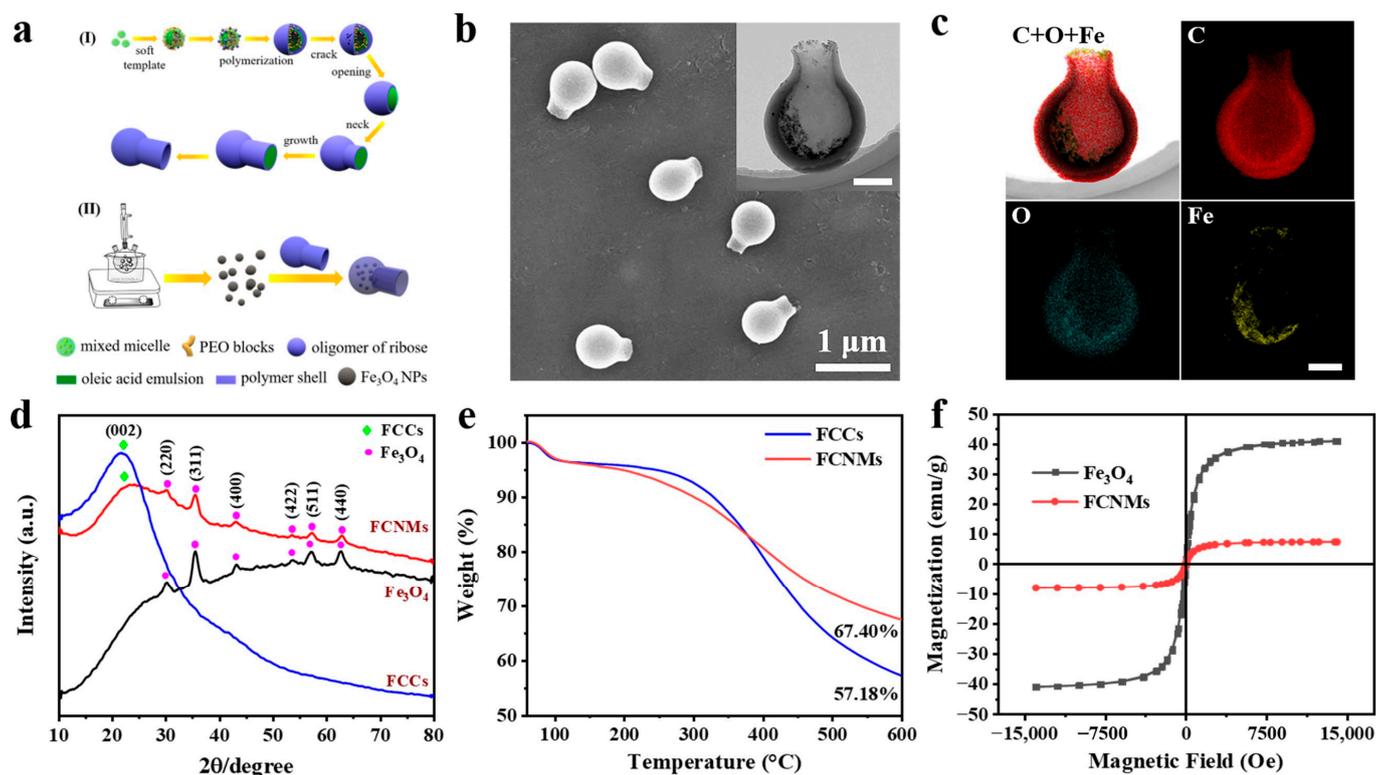
**Figure 2.** Fabrication and characterizations of the FCNMs. (**a**) Schematic illustration of the experimental procedures. (**b**) SEM image of as-prepared FCNMs (The inset is the TEM image of a typical FCNM. Scale bars: 200 nm.). (**c**) Corresponding EDX images of the distribution of C, O and Fe. Scale bars: 200 nm. (**d**) XRD patterns of the Fe_3O_4 NPs, FCCs and FCNMs. (**e**) TG curves of the FCCs and FCNMs. (**f**) Magnetic hysteresis loops of the Fe_3O_4 NPs and FCNMs.

3.3. Motion Behaviors of the FCNMs at Different pH Values

By virtue of the dual enzyme-like activities of Fe_3O_4 NPs that can react with H_2O_2 to produce •OH in acidic environment (peroxidase-like activity) and O_2 in near neutral and alkaline environments (catalase-like activity), it is conceivable that the as-prepared FCNMs could exhibit pH-dependent motion behaviors. In term of this, we explored the motion behaviors of the FCNMs at 2.5 wt% H_2O_2 aqueous solution in physiological pH values ranging from 4.4 to 7.4 with a gradient of 0.6. Since H_2O_2 decomposition usually causes the pH change in solution, the motion behaviors were conducted in a 20 mM buffer solution and observed using an inverted optical microscope. In each case, at least 15 FCNMs were analyzed. Typical tracking trajectories of the FCNMs with, or without, H_2O_2 "fuel" are presented in Figure 3a. In the absence of H_2O_2, the FCNMs performed Brownian motion only (Video S1), while those with the presence of H_2O_2 exhibited active self-propulsion, indicating that the driving force for the motion derived from the reaction between FCNMs and H_2O_2. The motion behaviors of the FCNMs exhibited a non-linear change with increasing pH values, which was further verified by the mean-square-displacement (MSD) versus the time interval (Δt) curves, according to the extracted 2D coordinates along the trajectories (Figure 3b). Without adding H_2O_2, the linear relationship between the MSD and Δt indicated a typical Brownian diffusive motion. The parabolic MSD curves, when using H_2O_2 as the fuel, suggested directional self-propulsion of the FCNMs. In order to clarity the relationship, we calculated the average velocities (Figure 3c) and diffusion coefficients (Figure 3d) of the FCNMs versus the pH values, which suggested their self-adaptive pH responsiveness. The velocities of the FCNMs decreased with increasing pH values from 4.4 to 5.6, and then rose until pH value was up to 6.8 with a velocity of 7.42 ± 1.0 μm/s ($\approx$12.4 body lengths·s^{-1}), after which the velocities subsequently dropped when pH was 7.4 (Videos S2 and S3). A similar dependence could also be found in diffusion coefficients of

the FCNMs at different pHs calculated by the equation of $MSD = 4D_{eff}\Delta t$. This confirmed that the as-prepared FCNMs could self-regulate their velocities, by sensing pH values in the physiological range, which provided a possibility for their self-adaptive movement toward a specific pH.
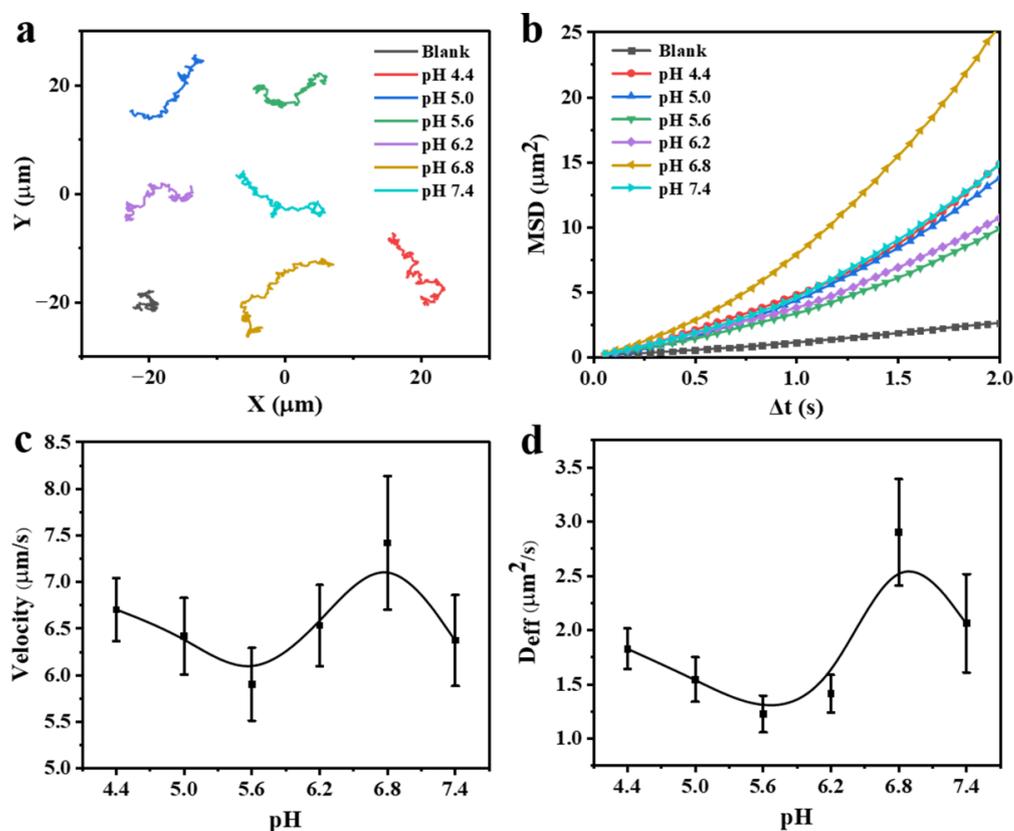

Figure 3. Motion analysis of the FCNMs at different pH values in 2.5 wt% H_2O_2 aqueous solution. (**a**) Track trajectories of the autonomous motion of the FCNMs in 10 s. (**b**) MSD curves versus Δt, (**c**) corresponding average velocities, and (**d**) average diffusion coefficients of the FCNMs.

3.4. Experimental Verification and Simulation Analysis for the pH-Responsive Mechanisms

In order to figure out why the FCNMs could exhibit pH-responsive motion behavior, we conducted a deep exploration for propulsion mechanisms through experimental verification and simulation analysis. The relationship between the dual enzyme-like activities of Fe_3O_4 NPs and environmental pH was studied firstly. The peroxidase-like activity of Fe_3O_4 NPs was tested by catalyzing the oxidation of substrate 3,3′,5,5′-tetramethylbenzidine (TMB) in the presence of H_2O_2, which was accompanied by color change to blue and appeared as obvious UV-Vis absorption at 650 nm (Figure S8). The results showed that the peroxidase-like activity increased with increasing H_2O_2 concentrations and reached the maximum at 2.5 wt%, whereas it decreased with increasing the pH values till at pH 7.4 there was no •OH production. Instead, when pH > 5.6, O_2 generation could be detected by monitoring dissolved oxygen in the reaction system, indicating the catalase-like activity of the as-synthesized Fe_3O_4 NPs. Then, we focused on verifying whether this law held true once the Fe_3O_4 NPs were encapsulated in a confined space to form a motor. The changes of the light absorption value at 650 nm in the first 1000 s of the reaction system were plotted in Figure 4a. It could be found that as the pH increased, the slope values in the linear range decreased and became zero once the pH exceeded 6.8, and, at the same time, the amounts of O_2 generation increased (Figure 4b). This suggested that, with increase of the pH values, Equations (7) and (8) could be activated to expend •OH, resulting in the decrease until it disappeared in the system. Further increasing the pH values, O_2, instead of •OH, became the main product. Therefore, in terms of the results it was concluded that with increasing

pH values from 4.4 to 7.4, the main products of the system experienced three stages: only •OH generated, •OH and O_2 coexisted, and O_2 dominated. This undoubtedly led to the transformation of propulsion mechanisms.
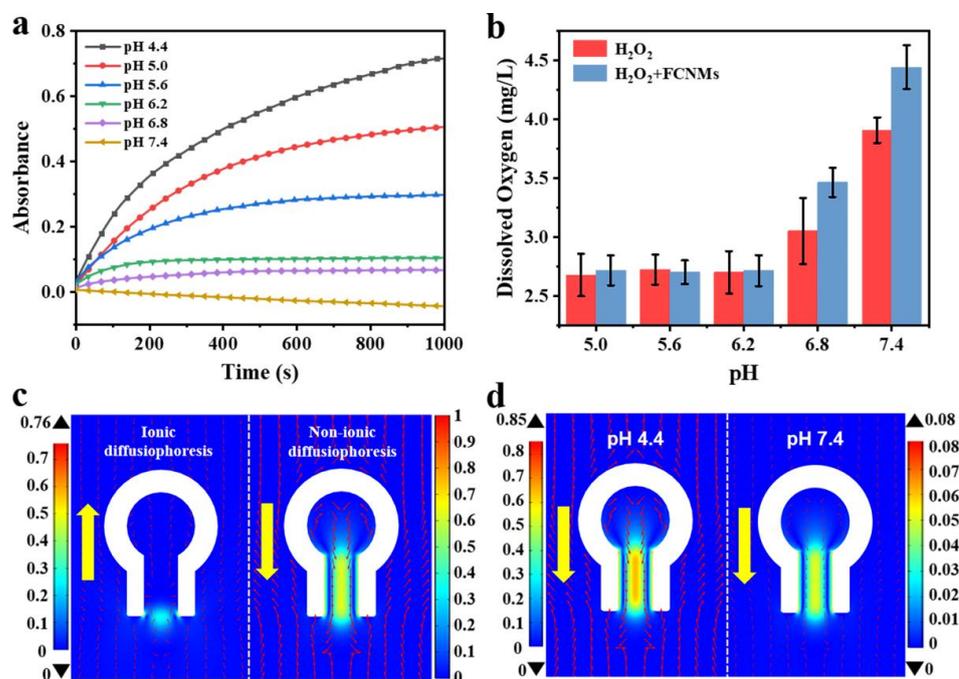

Figure 4. Verifications of propulsion mechanisms of the FCNMs through experiments and numerical simulations. (**a**) UV-Vis absorption-time course curves at 650 nm of the TMB-H_2O_2 system with the FCNMs at different pH values. (**b**) Dissolved oxygen analysis of the H_2O_2 system with or without the FCNMs at different pH values for 10 min. (**c**) Flow fields caused by ionic and non-ionic concentration gradient around the FCNMs at pH 4.4, respectively, where the small red arrows refer to the relative strength of flow velocity and the large yellow arrows refer to the direction of motion. (**d**) Total flow fields around the FCNMs at pH 4.4 and 7.4, respectively.

To further elucidate the self-adaptive pH-responsive motion behaviors of the FCNMs, we simulated the flow field distributions at different pH values, respectively, using COM-SOL multiphysics based on a 2D model. On the basis of Figure 4a,b, only Equation (6) occurred at a lower pH (e.g., pH < 5.6), •OH was the main product accompanied by the generation of OH^- (Figure S9). In order to exclude the effect of OH^- on the pH value, Equation (9) occurred and the ionic product $C_6H_7O_7^-$ was generated. Therefore, the FC-NMs in this case were co-driven by ionic and non-ionic diffusiophoresis. As shown in Figure 4c, the ionic concentration gradient formed at the opening, while the non-ionic concentration gradient was at the inner neck in an opposite direction. Therefore, the motion direction of the FCNMs depended on their relative magnitude. The simulated result showed that non-ionic diffusiophoresis played a dominant role in the current system, which drove the motor moving toward the flask mouth direction (Figure 4d). Limited by the resolution of the used optical microscope, the motion direction of the as-prepared FCNMs could not be distinctly resolved. Therefore, we treated much larger FCCs with a similar structure (~1 μm) to fabricate micromotors to experimentally verify the motion direction (Figure S10 and Video S4), which was in good agreement with the simulated result, and suggested the dominant effect of non-ionic diffusiphoresis. The reduced motion velocity in acidic pH from 4.4 to 5.6 could be attributed to the reduction of peroxidase-like activity of Fe_3O_4 NPs. When the pH value was up to 5.6, Equations (7) and (8) were activated to not only consume •OH groups but also to produce H^+, which was evidenced by the appearance of dissolved O_2 in the system. At this time, OH^- ions produced from Equation (6) were partly neutralized by H^+ ions giving rise to the reduction of ion concentrations, and

thus weakening the ionic diffusiophoresis. Additionally, O_2 generation could, to some extent, increase the non-ionic dissusiophoresis, and, thus, accelerate the FCNMs. With the disappearance of ionic diffusiophoresis in the system and the complete conversion of •OH groups, in terms of Equation (8), the movement velocity of the FCNMs reached a maximum at pH 6.8. The subsequently reduction of the velocity in near alkaline range might derive from the relatively low O_2 concentration gradient (Figure S11) and the diffusion restriction of the flask-like structures. From the point of view of the relative strength of the flow fields, we could also find that the non-ionic diffusiophoresis from •OH was much stronger than that of O_2, which was in keeping with their concentration gradient distribution and the experimental motion behavior.

3.5. Motion Behaviors of the FCNMs at Different H_2O_2 Concentrations

Figure 5 presents the effect of H_2O_2 concentrations on the motion behaviors of the as-prepared FCNMs. In each case, at least 15 FCNMs were analyzed. The results display that the FCNMs at 0 wt% H_2O_2 performed Brownian motion only, while those with the presence of H_2O_2 exhibited active self-propulsion with various trajectories, dependent on the H_2O_2 concentrations (Figure 5a). Parabolic MSD curves in Figure 5b show increasing slope values in the linear range until the H_2O_2 concentration was up to 2.5 wt%, also suggesting a transition from Brownian diffusive motion to self-propulsion. We also calculated the average velocities and diffusion coefficients of the FCNMs versus the H_2O_2 concentrations. The mobility of the FCNMs continued to increase with increasing H_2O_2 concentrations at the beginning, and dropped obviously when the H_2O_2 concentration was higher than 2.5 wt% (Figure 5c,d). It is suggested that more H_2O_2 might increase the ionic strength in the system, which had a negative effect on the motor movement. This phenomenon is consistent with the description of Sen et al., where it was proposed that when the total ionic strength of the system increases, there is a great negative effect on the motion capability of the motors driven by ionic diffusiophoresis [34]. The typical video of the FCNM swimming in 2.5 wt% H_2O_2 aqueous solution is provided in Video S5 with a maximum average velocity of 7.01 ± 0.59 µm/s ($\approx$11.7 body lengths·s^{-1}).
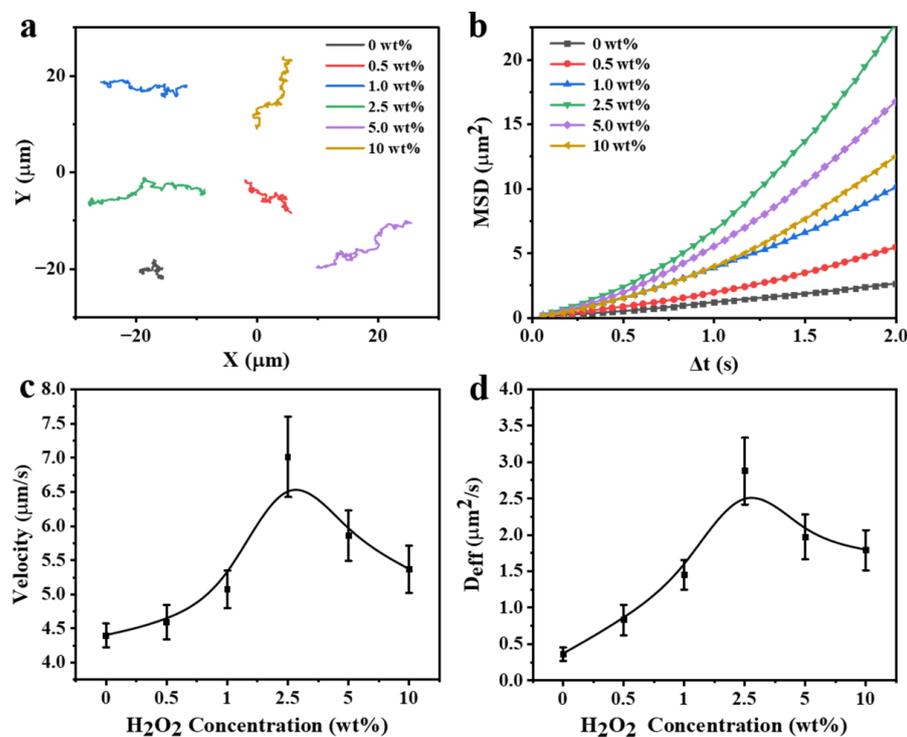
Figure 5. Motion analysis of the FCNMs at different H_2O_2 concentrations. (**a**) Track trajectories of the autonomous motion of the FCNMs in 10 s. (**b**) MSD curves versus Δt, (**c**) corresponding average velocities, and (**d**) average diffusion coefficients at different H_2O_2 concentrations.

3.6. Chemotactic Motion and Magnetic Responsiveness of the FCNMs

Thanks to the unique pH-responsive motion behaviors of FCNMs in the physiological range, they can display a self-adaptive chemotaxis motion toward a specific pH where they exhibit a maximum velocity. As shown in Figure 6a, a left-to-right gradually decreasing pH gradient was constructed by using a saturated agar filled with fuel solution at pH 6.8, which was placed on the other side of the mixed solution at pH 7.4 containing the FCNMs. In the presence of 2.5 wt% H_2O_2, the tracking trajectories of the 10 FCNMs were observed, and are depicted in Figure 6a. They all exhibited chemotactic behavior from pH 7.4 to 6.8 (Video S6). Moreover, acceleration phenomena in the process of getting closer to the agar were observed for the 10 FCNMs by calculating their real-time velocities (Figure 6b). The average velocities of the corresponding FCNMs in the first 10 s and the last 10 s were also calculated in Figure S12. To avoid any accidental effect, we cleverly set up an opposite pH gradient to observe the motion direction of the FCNMs positioned on the side of the mixed solution at pH 6.8. As expected, the FCNMs were far away from the saturated agar filled with fuel solution at pH 7.4 (Figure S13 and Video S7). Therefore, the results provided a direction control strategy for the as-prepared FCNMs, which was capable of actively targeting a specific area with a unique pH value. Besides this, on-demand direction manipulation could also be achieved by external magnetic field because of the inherent superparamagnetism of Fe_3O_4 NPs (Figure 6c). Facilely magnetic separation and easy re-dispersion features also endowed the as-prepared FCNMs with excellent recycling characters (Figure 6d).
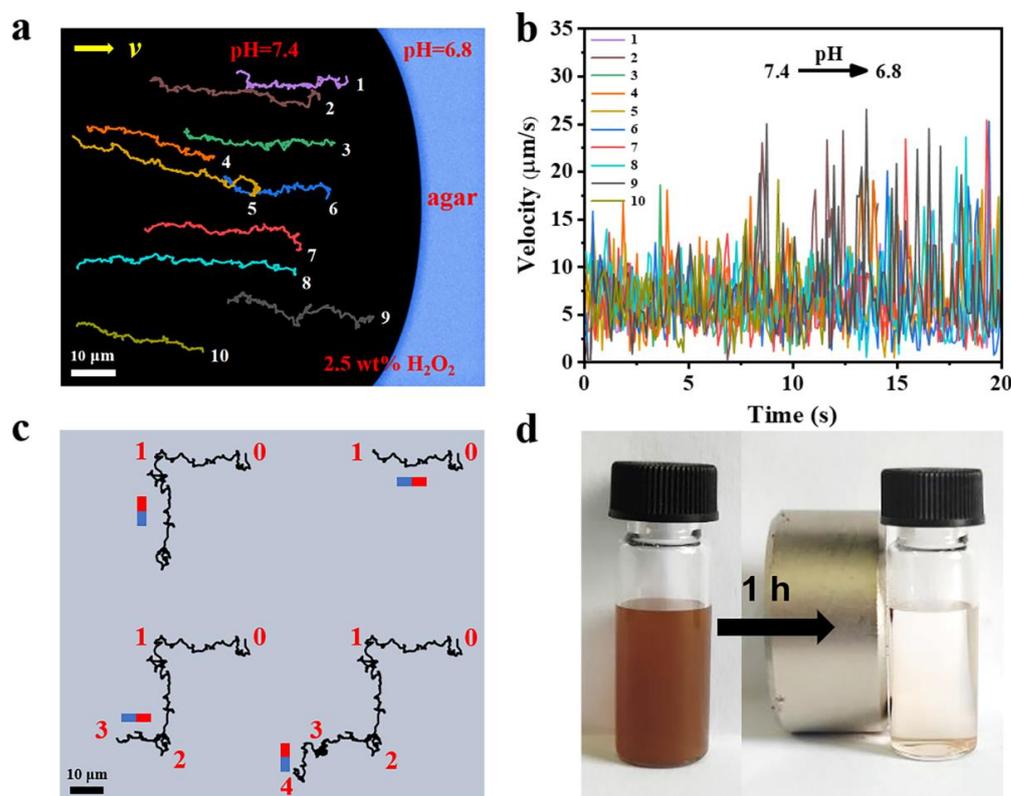
Figure 6. Chemotactic motion of the as-prepared FCNMs from pH 7.4 to 6.8 and magnetic responsiveness of the FCNMs. (**a**) The chemotactic track trajectories of the FCNMs in two pH environments in 30 s. (**b**) Real-time velocities for different FCNMs in 20 s. (**c**) Motion trajectories of a typical FCNM in 2.5 wt% H_2O_2 aqueous solution at pH 6.8 under magnetic manipulation. (**d**) Photograph of the FCNMs dispersed in aqueous solution and their magnetic separation for about 1 h.

4. Conclusions

In this work, we have demonstrated flask-like carbonaceous nanomotors (FCNMs) exhibiting self-adaptiveness toward a specifically physiological pH on the basis of the dual enzyme-like activities of magnetic Fe_3O_4 NPs. In the process of increasing pH in the physiological range from 4.4 to 7.4, the peroxidase-like activity for Fe_3O_4 NPs gradually wears off, accompanied by enhanced catalase-like activity, resulting in a transformation of the propulsion mechanisms from non-ionic and ionic diffusiophoresis to single non-ionic diffusiophoresis, which ultimately feeds back to a non-linear responsiveness upon pH. This endows the FCNMs with a unique chemotaxis towards a slightly acidic region (pH 6.8) that is a specific pH for generally physiological focal sites, such as tumor microenvironments. These results provide a design strategy for MNMs exhibiting a self-adaptive physiological pH-responsive motion, and the characteristic pH taxis, as well as the magnetic control, also offer a larger possibility in future biotechnological applications, especially for actively targeted tumor therapy.

Supplementary Materials: The following supporting information can be downloaded at: https://www.mdpi.com/article/10.3390/nano12122049/s1, Figure S1: Meshing conditions of the theoretical model. Figure S2: Characterizations of the FCCs. Figure S3: Characterizations of the Fe_3O_4@OA NPs synthesized at different aging temperatures. Figure S4: Characterizations of the Fe_3O_4@OA NPs synthesized at different aging time. Figure S5: Characterizations of the Fe_3O_4@OA NPs synthesized at different raw material molar ratios between oleyl alcohol and oleic acid. Figure S6: Relative peroxidase-like activities of the as-synthesized Fe_3O_4@OA NPs calculated by taking the group with the highest activity as 100%. Figure S7: Characterizations of oil-soluble Fe_3O_4@OA and water-soluble Fe_3O_4@DMSA NPs. Figure S8: Verifications of dual enzyme-like activities of Fe_3O_4@DMSA NPs. Figure S9: Verification of OH^- product by monitoring the change of pH values of pure 2.5 wt% H_2O_2 aqueous solution, FCNMs aqueous solution and their mixed solutions in 30 min. Figure S10: Time-lapse images of a comparable FCNM with a larger size of ~1 μm at pH 4.4. Figure S11: Concentration gradient distributions of ●OH, $C_6H_7O_7{}^-$ and O_2 on the symmetric axis of the FCNMs. Figure S12: A discrete distribution of the average velocities of different chemotactic FCNMs in the first 10 s and last 10 s. Figure S13: Chemotactic track trajectories of the FCNMs in a right-to-left gradually decreasing pH gradient at 2.5 wt% H_2O_2 in 30 s. Table S1: Typical parameters used in the simulations. Table S2: Average size, saturation magnetization (Ms) and relative peroxidase-like activity of as-synthesized different Fe_3O_4@OA NPs. Video S1: The FCNM moving in 0 wt% H_2O_2 aqueous solution. Video S2: The FCNM moving in 2.5 wt% H_2O_2 aqueous solution at pH 5.6. Video S3: The FCNM moving in 2.5 wt% H_2O_2 aqueous solution at pH 6.8. Video S4: The FCNM with a larger size moving in 2.5 wt% H_2O_2 aqueous solution at pH 4.4 for observing its motion direction. Video S5: The FCNM moving in 2.5 wt% H_2O_2 aqueous solution. Video S6: The FCNMs moving in 2.5 wt% H_2O_2 aqueous solution with a left-to-right gradually decreasing pH gradient. Video S7: The FCNMs moving in 2.5 wt% H_2O_2 aqueous solution with a right-to-left gradually decreasing pH gradient.

Author Contributions: Investigation, T.G.; software, J.L.; data curation and writing—original draft preparation, T.G. and L.X.; writing—review and editing, T.G., L.X. and J.G.; conceptualization and supervision, L.X. and J.G. All authors have read and agreed to the published version of the manuscript.

Conflicts of Interest: The authors declare no conflict of interest.

References

1. Zhang, Y.; Hess, H. Chemically-powered swimming and diffusion in the microscopic world. *Nat. Rev. Chem.* **2021**, *5*, 500–510. [CrossRef]
2. Wang, L.; Hao, X.; Gao, Z.; Yang, Z.; Long, Y.; Luo, M.; Guan, J. Artificial nanomotors: Fabrication, locomotion characterization, motion manipulation, and biomedical applications. *Interdisc. Mater.* **2022**, *1*, 256–280. [CrossRef]

3. Wu, J.; Balasubramanian, S.; Kagan, D.; Manesh, K.M.; Campuzano, S.; Wang, J. Motion-based DNA detection using catalytic nanomotors. *Nat. Commun.* **2010**, *1*, 36. [CrossRef] [PubMed]

4. Fu, S.; Zhang, X.; Xie, Y.; Wu, J.; Ju, H. An efficient enzyme-powered micromotor device fabricated by cyclic alternate hybridization assembly for DNA detection. *Nanoscale* **2017**, *9*, 9026–9033. [CrossRef] [PubMed]

5. Llopis-Lorente, A.; Garcia-Fernandez, A.; Murillo-Cremaes, N.; Hortelao, A.C.; Patino, T.; Villalonga, R.; Sancenon, F.; Martinez-Manez, R.; Sanchez, S. Enzyme-Powered Gated Mesoporous Silica Nanomotors for On-Command Intracellular Payload Delivery. *ACS Nano* **2019**, *13*, 12171–12183. [CrossRef]

6. Tang, S.S.; Zhang, F.Y.; Gong, H.; Wei, F.N.; Zhuang, J.; Karshalev, E.; de Avila, B.E.F.; Huang, C.Y.; Zhou, Z.D.; Li, Z.X.; et al. Enzyme-powered Janus platelet cell robots for active and targeted drug delivery. *Sci. Robot.* **2020**, *5*, eaba6137. [CrossRef]

7. de Avila, B.E.; Angsantikul, P.; Li, J.; Angel Lopez-Ramirez, M.; Ramirez-Herrera, D.E.; Thamphiwatana, S.; Chen, C.; Delezuk, J.; Samakapiruk, R.; Ramez, V.; et al. Micromotor-enabled active drug delivery for in vivo treatment of stomach infection. *Nat. Commun.* **2017**, *8*, 272. [CrossRef]

8. Vilela, D.; Blanco-Cabra, N.; Eguskiza, A.; Hortelao, A.C.; Torrents, E.; Sanchez, S. Drug-Free Enzyme-Based Bactericidal Nanomotors against Pathogenic Bacteria. *ACS Appl. Mater. Interfaces* **2021**, *13*, 14964–14973. [CrossRef]

9. Wang, L.; Hortelao, A.C.; Huang, X.; Sanchez, S. Lipase-Powered Mesoporous Silica Nanomotors for Triglyceride Degradation. *Angew. Chem. Int. Ed.* **2019**, *58*, 7992–7996. [CrossRef]

10. Hortelao, A.C.; Simo, C.; Guix, M.; Guallar-Garrido, S.; Julian, E.; Vilela, D.; Rejc, L.; Ramos-Cabrer, P.; Cossio, U.; Gomez-Vallejo, V.; et al. Swarming behavior and in vivo monitoring of enzymatic nanomotors within the bladder. *Sci. Robot.* **2021**, *6*, eabd2823. [CrossRef]

11. Kagan, D.; Benchimol, M.J.; Claussen, J.C.; Chuluun-Erdene, E.; Esener, S.; Wang, J. Acoustic Droplet Vaporization and Propulsion of Perfluorocarbon-Loaded Microbullets for Targeted Tissue Penetration and Deformation. *Angew. Chem. Int. Ed.* **2012**, *51*, 7519–7522. [CrossRef] [PubMed]

12. Kong, L.; Rohaizad, N.; Nasir, M.Z.M.; Guan, J.; Pumera, M. Micromotor-Assisted Human Serum Glucose Biosensing. *Anal. Chem.* **2019**, *91*, 5660–5666. [CrossRef] [PubMed]

13. Feng, Y.; Yuan, Y.; Wan, J.; Yang, C.; Hao, X.; Gao, Z.; Luo, M.; Guan, J. Self-adaptive enzyme-powered micromotors with switchable propulsion mechanism and motion directionality. *Appl. Phys. Rev.* **2021**, *8*, 011406. [CrossRef]

14. Tu, Y.; Peng, F.; Sui, X.; Men, Y.; White, P.B.; van Hest, J.C.M.; Wilson, D.A. Self-propelled supramolecular nanomotors with temperature-responsive speed regulation. *Nat. Chem.* **2017**, *9*, 480–486. [CrossRef] [PubMed]

15. Ji, Y.; Lin, X.; Zhang, H.; Wu, Y.; Li, J.; He, Q. Thermoresponsive Polymer Brush Modulation on the Direction of Motion of Phoretically Driven Janus Micromotors. *Angew. Chem. Int. Ed.* **2019**, *58*, 4184–4188. [CrossRef] [PubMed]

16. Neri, D.; Supuran, C.T. Interfering with pH regulation in tumours as a therapeutic strategy. *Nat. Rev. Drug. Discov.* **2011**, *10*, 767–777. [CrossRef]

17. Bhuyan, T.; Singh, A.K.; Dutta, D.; Unal, A.; Ghosh, S.S.; Bandyopadhyay, D. Magnetic Field Guided Chemotaxis of iMushbots for Targeted Anticancer Therapeutics. *ACS Biomater. Sci. Eng.* **2017**, *3*, 1627–1640. [CrossRef]

18. Dey, K.K.; Bhandari, S.; Bandyopadhyay, D.; Basu, S.; Chattopadhyay, A. The pH Taxis of an Intelligent Catalytic Microbot. *Small* **2013**, *9*, 1916–1920. [CrossRef]

19. Singh, A.K.; Dey, K.K.; Chattopadhyay, A.; Mandal, T.K.; Bandyopadhyay, D. Multimodal chemo-magnetic control of self-propelling microbots. *Nanoscale* **2014**, *6*, 1398–1405. [CrossRef]

20. Rayaroth, M.P.; Oh, D.; Lee, C.S.; Kumari, N.; Lee, I.S.; Chang, Y.S. Carbon-nitride-based micromotor driven by chromate-hydrogen peroxide redox system: Application for removal of sulfamethaxazole. *J. Colloid Interface Sci.* **2021**, *597*, 94–103. [CrossRef]

21. Su, Y.; Ge, Y.; Liu, L.; Zhang, L.; Liu, M.; Sun, Y.; Zhang, H.; Dong, B. Motion-Based pH Sensing Based on the Cartridge-Case-like Micromotor. *ACS Appl. Mater. Interfaces* **2016**, *8*, 4250–4257. [CrossRef] [PubMed]

22. Gao, W. Water-driven-micromotors. *ACS Nano* **2012**, *6*, 8432–8438. [CrossRef] [PubMed]

23. Gao, W.; D'Agostino, M.; Garcia-Gradilla, V.; Orozco, J.; Wang, J. Multi-fuel driven Janus micromotors. *Small* **2013**, *9*, 467–471. [CrossRef]

24. Jin, D.; Yu, J.; Chan, K.H.; Zhang, L. Self-propelled magnesium based micromotors: Synthesis and magnetic steering. In Proceedings of the International Symposium of Optomechatronics Technology (ISOT 2015), Neuchatel, Switzerland, 14–16 October 2015.

25. Li, M.; Li, D. Self-propulsion of aluminum particle-coated Janus droplet in alkaline solution. *J. Colloid Interface Sci.* **2018**, *532*, 657–665. [CrossRef] [PubMed]

26. Cui, Q.; Le, T.-H.; Lin, Y.-J.; Miao, Y.-B.; Sung, I.T.; Tsai, W.-B.; Chan, H.-Y.; Lin, Z.-H.; Sung, H.-W. A self-powered battery-driven drug delivery device that can function as a micromotor and galvanically actuate localized payload release. *Nano Energy* **2019**, *66*, 104120. [CrossRef]

27. Gao, S.; Hou, J.; Zeng, J.; Richardson, J.J.; Gu, Z.; Gao, X.; Li, D.; Gao, M.; Wang, D.-W.; Chen, P.; et al. Superassembled Biocatalytic Porous Framework Micromotors with Reversible and Sensitive pH-Speed Regulation at Ultralow Physiological H_2O_2 Concentration. *Adv. Funct. Mater.* **2019**, *29*, 1808900. [CrossRef]

28. Guo, Z.; Wang, T.; Rawal, A.; Hou, J.; Cao, Z.; Zhang, H.; Xu, J.; Gu, Z.; Chen, V.; Liang, K. Biocatalytic self-propelled submarine-like metal-organic framework microparticles with pH-triggered buoyancy control for directional vertical motion. *Mater. Today* **2019**, *28*, 10–16. [CrossRef]

29. Liu, L.; Dong, Y.; Sun, Y.; Liu, M.; Su, Y.; Zhang, H.; Dong, B. Motion-based pH sensing using spindle-like micromotors. *Nano Res.* **2016**, *9*, 1310–1318. [CrossRef]

30. Kim, B.H.; Lee, N.; Kim, H.; An, K.; Park, Y.I.; Choi, Y.; Shin, K.; Lee, Y.; Kwon, S.G.; Na, H.B.; et al. Large-scale synthesis of uniform and extremely small-sized iron oxide nanoparticles for high-resolution T1 magnetic resonance imaging contrast agents. *J. Am. Chem. Soc.* **2011**, *133*, 12624–12631. [CrossRef]

31. Chen, Z.P.; Zhang, Y.; Zhang, S.; Xia, J.G.; Liu, J.W.; Xu, K.; Gu, N. Preparation and characterization of water-soluble monodisperse magnetic iron oxide nanoparticles via surface double-exchange with DMSA. *Colloids Surf. A Physicochem. Eng. Asp.* **2008**, *316*, 210–216. [CrossRef]

32. Gao, C.; Zhou, C.; Lin, Z.; Yang, M.; He, Q. Surface Wettability-Directed Propulsion of Glucose-Powered Nanoflask Motors. *ACS Nano* **2019**, *13*, 12758–12766. [CrossRef] [PubMed]

33. Zhou, C.; Gao, C.; Lin, Z.; Wang, D.; Li, Y.; Yuan, Y.; Zhu, B.; He, Q. Autonomous Motion of Bubble-Powered Carbonaceous Nanoflask Motors. *Langmuir* **2020**, *36*, 7039–7045. [CrossRef] [PubMed]

34. Dey, K.K.; Sen, A. Chemically Propelled Molecules and Machines. *J. Am. Chem. Soc.* **2017**, *139*, 7666–7676. [CrossRef] [PubMed]